

# Application of the RMF mass model to the $r$ -process and the influence of mass uncertainties

B. Sun<sup>1,2\*</sup>, F. Montes<sup>2,3</sup>, L.S. Geng<sup>1,4</sup>, H. Geissel<sup>2</sup>, Yu.A. Litvinov<sup>2</sup> and J. Meng<sup>1,5,6,7</sup> <sup>†</sup>

<sup>1</sup>*School of Physics and State Key Laboratory of Nuclear Physics and Technology,  
Peking University, 100871 Beijing, China*

<sup>2</sup>*Gesellschaft für Schwerionenforschung GSI, 64291 Darmstadt, Germany*

<sup>3</sup>*National Superconducting Cyclotron Laboratory,  
Michigan State University, E. Lansing, MI 48824, USA*

<sup>4</sup>*Departamento de Física Teórica and IFIC, Centro Mixto,*

*Institutos de Investigación de Paterna - Universidad de Valencia-CSIC*

<sup>5</sup> *Department of Physics, University of Stellenbosch, Stellenbosch, South Africa*

<sup>6</sup>*Institute of Theoretical Physics, Chinese Academy of Sciences, Beijing, China*

<sup>7</sup>*Center of Theoretical Nuclear Physics,  
National Laboratory of Heavy Ion Accelerator, 730000 Lanzhou, China*

(Dated: November 7, 2018)

## Abstract

A new mass table calculated by the relativistic mean field approach with the state-dependent BCS method for the pairing correlation is applied for the first time to study  $r$ -process nucleosynthesis. The solar  $r$ -process abundance is well reproduced within a waiting-point approximation approach. Using an exponential fitting procedure to find the required astrophysical conditions, the influence of mass uncertainty is investigated.  $R$ -process calculations using the FRDM, ETFSI-Q and HFB-13 mass tables have been used for that purpose. It is found that the nuclear physical uncertainty can significantly influence the deduced astrophysical conditions for the  $r$ -process site. In addition, the influence of the shell closure and shape transition have been examined in detail in the  $r$ -process simulations.

PACS numbers: 21.10.-k, 21.10.Dr, 21.60.-n, 21.60.Jz, 23.40.-s, 26.30.Hj

---

\* B.Sun@gsi.de

<sup>†</sup> mengj@pku.edu.cn

## I. INTRODUCTION

It is of the utmost interest to explore the “terra incognita” of exotic nuclei, as evidenced by the fact that several Radioactive Ion Beam (RIB) facilities are being upgraded, under construction or planned to be constructed worldwide. Such investigations of the properties of these exotic nuclei, which may behave very differently from the nuclei around the  $\beta$ -stability line, result in new discoveries such as the halo phenomenon [1, 2] - nucleons spread like a thin mist around the nucleus, which can significantly increase the nuclear reaction ratio. Stellar nucleosynthesis processes such as the  $r$ -process [3, 4], which is responsible for roughly half of the enrichment of elements heavier than iron in the universe, also require a thorough understanding of the properties of exotic nuclei. Key properties like masses for example, determine the path that the nucleosynthesis process follow in the nuclei chart. Nevertheless, despite many experimental efforts, present knowledge of exotic nuclei still does not include much of what is required for a complete understanding of  $r$ -process nucleosynthesis. After the first systematic introduction to the  $r$ -process [5] half a century ago,  $r$ -process calculations for a long time could only rely on the phenomenological nuclear droplet mass formula [6] because of the lag of both experimental and theoretical development. Fortunately, in the last 15 year the theoretical study of nuclear properties has made tremendous progress and  $r$ -process calculations [7, 8, 9] have been carried out based on the refined droplet model FRDM [10], Hartree-Fock approach like ETFSI-Q [11], and the very recent microscopic rooted Hartree-Fock Bogliubov (HFB) [12, 13, 14].

Despite the progress in the theoretical nuclear structure physics, mass models predictions (which by design concentrate on different nuclear structure aspects) still show a large deviation when going to very neutron-rich nuclides, even though they have achieved similar quality to describe known nuclides. This is specially troublesome since the astrophysical scenario in which an  $r$ -process may occur is a matter of debate and all astrophysical simulations dedicated to the nature of the stellar environment depend on the input from nuclear physics. Mass model predictions, even in models that give similar global *rms* error still show local deviations differently.

In principle, microscopic-rooted mass models should have a more reliable extrapolation to the unknown regions, therefore these studies have received more and more interest as evidenced by the increasing number of non-relativistic HFB investigations [12, 13, 14, 15].

Based on a mass-driven fitted method, the latest HFB models have achieved a similar quality ( $rms \sim 0.7$  MeV) as the phenomenological FRDM mass model for known masses. More recently, another microscopic-rooted approach, the relativistic mean-field (RMF) theory [16] has received broad attention due to its successful description of several nuclear phenomena during the past years (for recent reviews, refer to Refs. [17, 18]). In the framework of the RMF theory, the nucleons interact via the exchanges of mesons and photons. The corresponding large scalar and vector fields, of the order of a few hundred MeV, provide simple and efficient descriptions of several important phenomena such as the large spin-orbit splitting, the density dependence of optical potential, the observation of approximate pseudo-spin symmetry, etc.. Moreover, the RMF theory can reproduce well the isotopic shifts in the Pb region [19], explain naturally the origin of the pseudo-spin symmetry [20, 21] as a relativistic symmetry [22, 23, 24, 25] and spin symmetry in the anti-nucleon spectrum [26].

The first RMF mass table was reported in Ref. [27] for 2174 even-even nuclei with  $8 \leq Z \leq 120$  but without including pairing correlations. Later on, the calculation was improved by adopting a constant-gap BCS method and calculated 1200 even-even nuclei with  $10 \leq Z \leq 98$  [28], most of which are close to the  $\beta$ -stability line. More recently, using the state-dependent BCS method with a  $\delta$ -force [29, 30], the first systematic study of the ground state properties of over 7000 nuclei ranging from the proton drip line to the neutron drip line was performed [31]. Comparison of this calculation with experimental data and to the predictions of other mass models will be presented in more detail in Sec II.

Considering the recent development of the microscopic mass models in both the HFB and RMF approach, it is very interesting to examine their applicability to an  $r$ -process calculation. The main goals of this paper is to explore to what extent the solar  $r$ -process abundance can be reproduced using the new RMF mass table [31] and by comparing with other theoretical mass models, to determine the influence of nuclear mass uncertainty in  $r$ -process calculations. The paper is organized as follows. In Sec. II the global agreement of the new RMF mass table with the experimental data is discussed and the RMF prediction in the very neutron-rich range is compared with the FRDM [10], the ETFSI-Q [11] and the latest HFB-13 [15] mass tables. In Sec. III, a short introduction to a site-independent  $r$ -process approach is given. In Sec. IV, the new mass table is applied to reproduce the solar  $r$ -process abundances. In addition, the result is compared to the  $r$ -process abundances obtained with the predictions of the FRDM, ETFSI-Q and HFB-13 mass models. Finally

the summary and conclusions are given in Sec. V.

## II. GLOBAL BEHAVIOR OF THE NEW RMF MASS TABLE

With about 10 parameters fitted to the ground-state properties of around 10 spherical nuclei, the RMF approach with the TMA parameter set is found to give a satisfactory description for all the nuclei in the nuclear chart. The model deviation of one-neutron separation energy  $S_n$  with respect to the known experimental data can be characterized by the *rms* deviation ( $\sigma_{rms}$ )

$$\sigma_{rms} = \sqrt{\frac{1}{n} \sum_{i=1}^n (S_n^{\text{th}} - S_n^{\text{exp}})_i^2}, \quad (1)$$

Although a relatively large *rms* deviation for the absolute mass value is found for the RMF calculation in comparison with the FRDM and HFB-13 models, the finite differences in binding energies such as the practical used one-neutron separation energies  $S_n$  are well predicted due to the cancelation of systematic error [31, 32]. The *rms* deviation of  $S_n$  for the FRDM, ETFSI-Q, HFB-13 and RMF models with respect to experimentally values [33] are 399 keV, 528 keV, 546 keV and 654 keV, respectively. Here the comparisons include nuclei with  $Z, N \geq 8$ . Comparing the predictions of the RMF model to the known values [33] results in discrepancies between -1.4 MeV to 1 MeV, while the difference between either the FRDM or the HFB-13 and the experimental data is in the range of -1.3 MeV to 0.5 MeV. It shows that the microscopic model such as the RMF approach can almost achieve the same level of accuracy for known one-neutron separation energy  $S_n$  as the phenomenological FRDM. For each isobaric chain with mass  $A$ , the distance between the nuclide  $(Z, A)$  and the nuclide  $(Z_0, A)$  in the  $\beta$ -stability line [34] is defined by  $\varepsilon = Z_0 - Z$  with

$$Z_0 = \frac{A}{1.98 + 0.0155A^{2/3}}, \quad (2)$$

i.e.,  $\varepsilon = 0$  stands for the most stable nuclei and  $\varepsilon > 0$  the neutron-rich nuclei. The *rms* deviation  $\sigma_{rms}$  of  $S_n$  as a function of  $\varepsilon = Z_0 - Z$  for different mass models is shown in Fig. 1. It is remarkable that almost the same order of prediction power of  $S_n$  from the neutron-deficient side to the neutron-rich side is achieved for all the models, even though models like FRDM and HFB-13 have about 10 more free parameters than the RMF model and were optimized for all the known masses. While the macroscopic-microscopic mass model FRDM

shows the best agreement with experimental values in the neutron deficient mass region, it gets progressively worse when moving away from the stability line towards the neutron-rich side.

All theoretical models addressing nuclei far away from the  $\beta$ -stability line involve a dramatic extrapolation to unknown nuclei. Thus it is interesting to examine what is the difference of  $S_n$  predicted in the different models when going towards the neutron-rich side. In Fig. 2, the differences between  $S_n$  in the RMF model and those in the HFB-13 mass models are shown as an example. In general, most of the discrepancies between the two microscopic models range from -1 MeV to 1 MeV across the entire nuclear chart. Furthermore, the  $S_n$  value is consistent with that in the HFB-13 model in the range of -0.5 MeV to 0.5 MeV when going to the unknown region of the nuclei chart. These differences indicate that the extrapolation can be quite different depending on the underlying physics of the model. Similar conclusion can be drawn also for the comparison of the RMF and FRDM models. Around the  $N = 82$  shell, the RMF model predicts a systematic lower  $S_n$ . These different  $S_n$  predictions towards the neutron drip line affect  $r$ -process calculations and thus the corresponding determined astrophysical conditions.

The evolution of the nuclear structure around the shell closures  $N = 82$  and 126 is critical in understanding the  $r$ -process abundance distribution around the  $A = 130$  and  $A = 195$  abundance peaks. At the shell closures, the one-neutron separation energy drops, and thus the corresponding nucleus in the  $r$ -process path cannot absorb another neutron without photo-disintegration. Therefore it has to “wait” for the  $\beta$ -decay to proceed, and the path moves closer to the valley of stability where the half-lives are longer. These isotopes with long half-lives serve as bottlenecks of the process where abundances accumulate and the abundance peaks are formed. In Fig. 3, the predicted average one-neutron separation energy  $S_{2n}/2$  around  $N = 82$  in the RMF model is displayed as a function of mass number for isotopes from Kr to Ba together with the experimental values and the predictions of the FRDM, ETFSI-Q and HFB-13 models. The dominating isotopes in the  $r$ -process path (defined as waiting points and discussed in Sec. IV) are also indicated for the corresponding mass model. Similarly, Fig. 4 presents  $S_{2n}/2$  distribution around  $N = 126$  shell for isotopes from Ce to Pt. In general, the RMF model reproduces well the experimental data, and predicts a much subtle variance relative to other mass models. The neutron shell gaps, defined as  $\Delta_n(Z, A) = S_{2n}(Z, A) - S_{2n}(Z, A + 2)$ , can be more clearly seen from Fig. 5,

which shows the shell gaps for  $N = 82$  and  $126$  in the RMF approach in comparison with the data available and those in the FRDM, ETFSI-Q and HFB-13 models. The nuclei in the shadowed area are in the  $r$ -process path. At the  $N = 82$  shell, all the mass models except the FRDM model show a strong quenching effect (i.e., the shell gap drops) towards the neutron-rich side. The RMF shell gap is overestimated compared with the data available and it is around 2 MeV larger than other models for  $45 \leq Z \leq 60$ . Regardless of this, the RMF model succeeds in predicting the enhanced double-magic effect at  $Z = 50$  together with the HFB-13 model. For  $N = 126$ , there is no sign of shell quenching observed in the  $r$ -process region for all the models. A unique feature of the RMF model is that it fully coincides with the available data and it is also the only model to reproduce the enhanced double-magic effect at  $Z = 82$ . In comparison, the other models fail to reproduce the trend of the known  $N = 126$  shell. Towards the neutron drip line, the RMF prediction tends to enhance the shell until the maximum is reached around  $Z = 60$  while the other models have a roughly constant shell gap.

### III. SITE-INDEPENDENT $r$ -PROCESS APPROACH

Since the  $r$ -process is responsible for the synthesis of half the heavier nuclei beyond the iron group [3, 4], the basis of the nucleosynthesis mechanism have been extensively studied. Nevertheless, the location where it occurs has not been unambiguously identified. Current location candidates include the neutrino-driven wind off a proton-neutron star in core collapse supernovae [35, 36, 37, 38], neutron star mergers [39, 40, 41], jets in core collapse supernovae [42], shocked surface layers of O-Ne cores [43], and gamma ray bursts [44]. Because the specific astrophysical conditions among the different scenarios may change, solar  $r$ -process abundances [45] have been used in the past to constrain the astrophysical conditions using a site-independent approach [7, 46]. In this approach seed-nuclei (usually the iron group) are irradiated by neutron sources of high and continuous neutron densities  $n_n$  ranging from  $10^{20}$  to  $10^{28} \text{ cm}^{-3}$  over a timescale  $\tau$  in a high temperature environment ( $T \sim 1\text{GK}$ ). This superposition of  $r$ -process components  $(n_n, \tau)$  is needed to reproduce the overall shapes and positions of the solar  $r$ -process abundances [7, 8, 47] and it is equivalent to the exponential neutron exposures in the  $s$ -process [48]. The configuration of many  $r$ -process components seems to be also a reasonable approximation to the real  $r$ -process event.

For instance, one can think of it as the “onion” structure of neutron sources with different densities, where the seed-nuclei capture neutrons while moving through different zones with different thicknesses. In this paper we explore for the first time the application of the new RMF mass model to an  $r$ -process calculation and at the same time investigate the effect of nuclear physics uncertainty in the  $r$ -process.

Due to the high neutron densities, neutron captures are much faster than the competing  $\beta$ -decays and an  $(n, \gamma) \rightleftharpoons (\gamma, n)$  equilibrium is nicely established for every element. The abundance ratio of two isotopes in the timescale  $\tau$  can be expressed simply as

$$\frac{Y(Z, A+1)}{Y(Z, A)} = n_n \left( \frac{h^2}{2\pi m_\mu \kappa T} \right)^{3/2} \frac{G(Z, A+1)}{2G(Z, A)} \left( \frac{A+1}{A} \right)^{3/2} \exp \left[ \frac{S_n(Z, A+1)}{\kappa T} \right], \quad (3)$$

where  $Y(Z, A)$  denotes the abundance of the nuclide  $(Z, A)$ ,  $S_n$  is the one-neutron separation energy,  $G(Z, A)$  is the partition function of nuclide  $(Z, A)$ , and  $h$ ,  $\kappa$  and  $m_\mu$  are the Planck constant, Boltzmann constant and atomic mass unit, respectively. Neglecting the difference in the ratios of the partition functions and the atomic mass, one can easily see that the isotopic abundance distribution  $P(Z, A)$  and the abundance maxima in each isotopic chain are determined by  $n_n$ ,  $T$  and  $S_n$ . Approximating  $Y(Z, A+1)/Y(Z, A) \simeq 1$  at the highest isotopic abundance for each element, and all other quantities being constant, the average neutron-separation energy  $\bar{S}_n$ , calculated by

$$\begin{aligned} \bar{S}_n &\approx \kappa T \log \left[ \frac{2}{n_n} \left( \frac{2\pi m_\mu \kappa T}{h^2} \right)^{3/2} \right] \\ &= T_9 \left\{ 2.79 + 0.198 \left[ \log \left( \frac{10^{20}}{n_n} \right) + \frac{3}{2} \log T_9 \right] \right\}, \end{aligned} \quad (4)$$

is the same for all the nuclides with the highest abundance in each isotopic chain.  $T_9$  denotes the temperature in  $10^9$  K. Higher temperature or lower neutron density will drive the  $r$ -process path towards the valley of stability. Due to the pairing correlation the most abundant isotope always has an even neutron number  $N$ .

If fission is neglected, the abundance flow from one isotopic chain to the next is governed by  $\beta$ -decays and can be expressed by a set of differential equations:

$$\begin{aligned} \frac{dY(Z, A)}{dt} &= Y(Z-1) \sum_A P(Z-1, A) \lambda_\beta^{Z-1, A} \\ &\quad - Y(Z) \sum_A P(Z, A) \lambda_\beta^{Z, A}, \end{aligned} \quad (5)$$

where  $\lambda_{\beta}^{Z,A}$  is the total decay rate of the nuclide  $(Z, A)$  via the  $\beta$ -decay and the delayed neutron emission, and  $Y(Z) = \sum_A Y(Z, A) = \sum_A P(Z, A)Y(Z)$  is the total abundance in each isotopic chain. Using Eqs. (3) and (5), the abundance for each isotope can be calculated. After the neutrons freeze out, all the isotopes will proceed to the corresponding stable isotopes via  $\beta$ -decays.

#### IV. CALCULATIONS

In the present calculation, unknown one-neutron separation energies  $S_n$  were calculated from the RMF approach [31] and  $\beta$ -decay properties were taken from Ref. [49]. Available experimental data [33, 50] was used when available. Similar to the method used in Refs. [8, 46, 47], we applied sixteen components with neutron densities in the range of  $10^{20}$ - $3 \times 10^{27}$   $\text{cm}^{-3}$  in our calculation. We chose a temperature  $T = 1.5$  GK. We assumed that for this temperature the irradiation time  $\tau$  and the corresponding weight  $w$  follow the exponential dependent of neutron density  $n_n$ , i.e.,

$$w(n_n) = n_n^a, \quad \tau(n_n) = b \times n_n^c, \quad (6)$$

where  $a, b, c$  are parameters to be fixed. These parameters can be obtained from a least-square fit to the solar  $r$ -process abundances. We further assume that the longest neutron irradiation time has to be longer than 0.5 s but shorter than 20 s. The exponential relations in Eq. (6) have been observed when fitting the three  $r$ -process peaks [51] and used for stellar and chronometers studies [8, 47, 52].

It was found that  $r$ -process components with  $\tau(n_n) = 0.454n_n^{0.040}$  s and  $w(n_n) = 2.1n_n^{0.02}$  best reproduce the solar  $r$ -process abundance. Fig. 6 shows the contribution of the four-group weighted  $r$ -process components after  $\beta$ -decays to the resulting best fit. The black solid curve with isotopic abundances normalized to  $A = 130$ , corresponds to the fit using all the sixteen components. The green, red, blue and grey dashed curves are the sum of the abundances calculated with  $\log(n_n)$  ranging from 20 to 22.5, 23 to 24.5, 25 to 26.5 and 27 to 27.5, respectively. The first six components with  $\log(n_n)$  between 20 and 22.5 seem to account for the  $A = 80$  abundance peak. The four components with  $\log(n_n)$  between 23 and 24.5 are responsible for the overall structure of the  $r$ -abundance curve beyond  $A = 120$  and the remaining components only improve the description of the theoretical calculation



for  $A > 150$ . In general, the fit is found to reproduce well the solar  $r$ -process abundances and also the position of the abundance peaks.

The  $r$ -process runs relatively close to the  $\beta$ -stability line around the shell closure, thus the experimentally known mass values around  $N = 82$  shell significantly influence the abundance distribution after the second abundance peak. Taking our best simulation using the RMF masses as an example, the ratio between the abundance at  $A = 130$  and the abundance at  $A = 195$  is 2.8 when taking the experimental data into account, and it increases to 24.6 if the experimental data are not used. The same ratio decreases from 4.0 to 1.3 for the best simulation using the FRDM masses (to be discussed below). In order to minimize the contribution from the theoretical uncertainty of known masses, experimental information was included in the calculations.

In order to investigate the impact of theoretical uncertainty of unknown masses in an  $r$ -process calculation, we also performed the same procedure using instead the FRDM, ETFSI-Q and HFB-13 mass predictions while keeping the same  $\beta$ -decay properties. The astrophysical conditions determined by using various mass inputs are shown in Fig. 7. The obtained superpositions of sixteen  $r$ -process components for all the mass tables are collected in table I. Similar to the astrophysical conditions obtained from ETFSI-Q simulations, the astrophysical condition using the RMF mass input requires a relatively constant weighting factor for different neutron densities. However, the FRDM and HFB-13 cases favor a large weighting factor for the low neutron density. As for the neutron irradiation time, the best RMF fit requires component durations of as long as 6 s while the FRDM and HFB-13 simulations only requires up to 1.5 s. The ETFSI-Q component durations are somewhat in between. Moreover, it may be worth mentioning that the simulations using the FRDM and HFB-13 masses demand almost identical astrophysical conditions. Using a lower temperature  $T = 1.35$  GK, a similar calculation based on the ETFSI-Q mass model is carried out in Ref. [47]. As shown in Fig. 7, their obtained neutron irradiation times are in good agreement with our calculation using the ETFSI-Q masses and FRDM half-life inputs, but the weighting factors differ. The superposition obtained in Ref. [47] demands a more sharp evolution of the weighting factor as a function of  $n_n$ . Since a lower temperature of  $T = 1.35$  GK in our calculations only weakly impacts the condition obtained, the difference should be due to the different  $\beta$ -decay properties used in that work. Based on a full dynamical network calculation, faster time-scales of the order of hundreds of milliseconds, are found in Ref. [53]

for an  $r$ -process in the neutron-wind scenario of core-collapse type II supernovae. However, this different time scale can be at least partially attributed to different seed nuclides. In their calculation, the  $r$ -process starts from a seed distribution containing neutron-rich nuclei with mass numbers between 80 and 100, while ours starts from  $^{56}\text{Fe}$ .

Calculated solar  $r$ -process abundances after  $\beta$ -decays using different mass models are displayed in Fig. 8. Shadowed areas show the regions with underproduced abundances before the neutrons freeze-out. After  $\beta$ -decays to the stability line, these gaps are too large to be completely filled in by  $\beta$ -delayed neutron emissions. It should be pointed out that the solar system  $r$ -process abundances are defined as the abundances not produced in the  $s$ -process and  $p$ -process that still have to be created elsewhere to explain the solar system abundances. Although it is thought that the  $r$ -process is responsible for the majority of those isotopic abundances with  $Z \geq 56$ , its contribution to the lighter elements is still debatable [57, 58]. It is possible that some of the discrepancies in the reproduction of the low mass abundances may be due to an additional nucleosynthesis component creating some of those abundances. However, since astrophysical conditions and nuclear properties both affect the resulting  $r$ -process abundances, one need to determine or at least understand the uncertainty in the nuclear physics properties in the future works to disentangle both effects [59]. In this paper we only discuss possible nuclear physics reasons for such underabundances.

$R$ -process abundances calculated with all nuclear mass models result in abundance underproduction at  $A \sim 120$  and  $A \sim 170$ . Traditionally, the underestimation of the isotopic abundances before  $A \sim 130$  peak has been attributed to the overestimated strength of the  $N = 82$  shell closure [8, 47, 51] in the theoretical nuclear physics model even though the experimental evidence is still debated [54, 55, 56]. Since it is not possible to do a complete study of the shell-quenching effect at the single particle level which should affect more nuclei than the one with  $N = 82$ , we only study the effect of a reduced shell closure by artificially decreasing the shell gap energies at  $N = 82$  in the RMF and FRDM models by 2 MeV and 1 MeV, respectively. In such a way, the shell gaps interested for the  $r$ -process would roughly have the same values as those in the quenched models ETFSI-Q and HFB-13. Eventually, a better agreement with the observation at  $A \sim 120$  is obtained as shown in Fig. 8(a-b). This can be easily understood as follows. A reduction of shell gap leads to a nuclear matter repopulation in the isotopic chain according to Eq. 3.  $R$ -process waiting points located at  $N = 82$  move closer to the valley of stability and thus some of the underabundance can be

filled. Furthermore, based on Fig. 3 one could expect that the quenched shell gap at  $N = 82$  would not affect the abundance around  $A \sim 115$ . It is interesting to note that the  $r$ -process simulation using the shell-quenched ETFSI-Q model in Fig. 8(c) show a good agreement with solar abundances pattern at  $A \sim 120$  together with a large underproduction at a lower mass number  $A \sim 115$ .

The abundance trough at  $A \sim 115$  for the FRDM, RMF and ETFSI-Q models can be related to the additional bump of  $S_n$  at  $A = 110 - 120$  in Fig. 3, and thus the associated nuclear shape transition. In the case of the ETFSI-Q model, nuclear shape changes for prolate to oblate and then to spherical nuclei with  $N = 82$ . This transition leads to a deviation from the approximate relationship between neutron separation energies and mass number for each isotope, and can be clearly recognized in Fig. 3(c) by the sudden increase of the separation energies. In order to see the sensitivity of the  $r$ -process calculation to the effect of the nuclear shape transition, we lowered the separation energies of  $^{118,120}\text{Mo}$  by 1 MeV in the ETFSI-Q model, but kept the other nuclear physics input unchanged. Those isotopes are in the  $r$ -process path and show a bump in the one-neutron separation energies as a function of mass number. As shown in Fig. 8(c) the  $A \sim 115$  trough is largely filled in. A similar analysis shows the same conclusion for the FRDM and RMF mass models. Although we have mainly focused in the underabundance below  $N = 82$ , similar conclusion can be drawn for the trough around  $A \sim 170$ . As an example, Fig. 8(c) shows that the trough is almost completely filled in by lowering the separation energies of  $^{185}\text{Pm}$  and  $^{186}\text{Sm}$  by 1 MeV. This suggests that the potentially wrongly assigned location of the shape transition before the neutron magic number in the theoretical predictions can lead to the troughs before the abundance peaks.

Of all the mass models, the HFB-13 is the only one that shows a smooth one-neutron separation energy change from Sr to Ru. As a result, the  $r$ -process waiting points are continuous and there is not apparent gap in the  $r$ -process path (see Fig. 3(d)). Only modifications in the nuclear masses would not result in the filling of the the abundance gap at  $A \sim 115$ . Such underproduction may be traced back to the  $\beta$ -decay properties. By increasing the  $\beta$ -decay half-lives of the critical nuclei  $^{113,115,117}\text{Y}$  by five times, we found that the trough before the  $A \sim 130$  peak in the HFB-13 case can be nearly filled in as shown in Fig. 8(d).

## V. SUMMARY

We have applied the most recent comprehensive mass models, the non-relativistic microscopic-rooted HFB-13 and the relativistic RMF in  $r$ -process calculations. For the sake of comparison, we also included the widely used macro-microscopic models FRDM and ETFSI-Q. Of these models, the HFB-13 and RMF models are used for the first time in such calculations. Based on a simple  $r$ -process model, it is found that all mass models reproduce the main features of the solar  $r$ -process pattern and the position of the abundance peaks. Since  $r$ -process simulations have to rely on predicted nuclear physics properties of unknown regions in the nuclear chart, we have compared the predictions of different mass models. We have also made a systematic study of the influence due to the mass model uncertainty in the application of the  $r$ -process and thus in the required astrophysical conditions. This nuclear physical uncertainty is very important for the complete understanding of the  $r$ -process since the results of more modern full dynamic  $r$ -process calculations depend on the nuclear mass input used. It is found that the deduced astrophysical conditions like the neutron irradiation time of the  $r$ -process can be significantly different depending on the mass model used. Among the different models, the simulation using the RMF masses requires a longer time scale (up to a factor of 4) than those using FRDM and HFB-13 models. Furthermore, it is found that the optimal astrophysical conditions obtained using the ETFSI-Q and RMF mass models require a relatively constant weighting factor for neutron densities in the range  $10^{22}$  to  $10^{28} \text{ cm}^{-3}$ , while the FRDM and HFB-13 simulations favor a large weighting factor at low densities. In addition, we have explored the possible deficiencies in different mass models, and found that the observed abundance underproduction before the abundance peaks in all the models can be a combined and complex effect of both shell structure and shape transition. An exception is the underproduction at  $A \sim 115$  in the HFB-13 model which can be attributed to incorrect  $\beta$ -decay rates. Future experiments are needed to determine the strength of the shell closure towards the neutron drip line as well as the precise locations of the shape transition toward the shell-closures.

## Acknowledgments

We thank C. Scheidenberger for his interest of this work, G. Martinez Pinedo and B. Pfeiffer for valuable discussions, J.M. Pearson for providing the ETFSI-Q and HFB-13 mass tables and P. Möller for the  $\beta$ -decay data. This work is partly supported by Major State Basic Research Developing Program 2007CB815000 as well as the National Natural Science Foundation of China under Grant No. 10435010, 10775004 and 10221003.

- 
- [1] I. Tanihata, et al., Phys. Rev. Lett. **55**, 2676 (1985).
  - [2] W. Schwab, et al., Z. Phys. A**350**, 283 (1995).
  - [3] J.J. Cowan, F.-K. Thieleman, and J.W. Truran, Phys. Rep. **208**, 267 (1991).
  - [4] Y.-Z. Qian, Prog. Part. Nucl. Phys. **50**, 153 (2003).
  - [5] E.M. Burbidge, G.R. Burbidge, W.A. Fowler, and F. Hoyle, Rev. Mod. Phys. **29**, 4 (1957).
  - [6] E.R. Hilf, H.V. Groote, and K. Takahashi, *in Proc. Third International Conference on Nuclei Far from Stability* (Geneva: CERN), 142 (1976).
  - [7] K.-L. Kratz, J.-P. Bitouzet, F.-K. Thielemann, P. Möller, and B. Pfeiffer, Astrophys. J., **403**, 216 (1993).
  - [8] B. Pfeiffer, K.-L. Kratz, and F.-K. Thielemann, Z. Phys. A **357**, 235 (1997).
  - [9] S. Wanajo, S. Goriely, M. Samyn, and N. Itoh, Astrophys. J. **606**, 1057 (2004).
  - [10] P. Möller, J.R. Nix, W.D. Myers, and W.J. Swiatecki, At. Data Nucl. Data Tables **59**, 185 (1995).
  - [11] J.M. Pearson, R.C. Nayak, and S. Goriely, Phys. Lett. **B387**, 455 (1996).
  - [12] S. Goriely, M. Samyn, P.-H. Heenen, J.M. Pearson, and F. Tondeur, Phys. Rev. C **66**, 024326 (2002).
  - [13] S. Goriely, M. Samyn, M. Bender, and J.M. Pearson, Phys. Rev. C **70**, 044309 (2004).
  - [14] M. Samyn, M. Bender, and J.M. Pearson, Phys. Rev. C **68**, 054325 (2003).
  - [15] S. Goriely, M. Samyn, and J.M. Pearson, Nucl. Phys. **A773**, 279 (2006).
  - [16] J.D. Walecka, Ann. Phys. (NY), **83**, 491 (1974).
  - [17] M. Bender, P.-H. Heenen, and P.G. Reinhard, Rev. Mod. Phys., **75**, 121 (2003).
  - [18] J. Meng, H. Toki, S.G. Zhou, S.Q. Zhang, W.H. Long, and L.S. Geng, Prog. Part. Nucl. Phys.,

- 57**, 470 (2006).
- [19] M.M. Sharma, G.A. Lalazissis, P. Ring, Phys. Lett. **B317**, 9 (1993).
  - [20] A. Arima, M. Harvery, and K. Shimizu, Phys. Lett. **B30**, 517 (1969).
  - [21] K.T. Hecht, and A. Adler, Nucl. Phys. **A137**, 129 (1969).
  - [22] J.N. Ginocchio, Phys.Rev.Lett., **78**, 436 (1997).
  - [23] J. Meng, K. Sugawara-Tanabe, S. Yamaji, P. Ring, and A. Arima, Phys. Rev. C **58**, 628(R) (1998).
  - [24] J. Meng, K. Sugawara-Tanabe, S. Yamaji, and A. Arima, Phys. Rev. C **59**, 154 (1999).
  - [25] T.S. Chen, H.F. Lu, J. Meng, S.Q. Zhang, and S.G. Zhou, Chin. Phys. Lett., **20**, 358 (2003).
  - [26] S.G. Zhou, J. Meng, P. Ring, Phys. Rev. Lett., **91**, 262501 (2003).
  - [27] D. Hirata, K. Sumiyoshi, I. Tanihata, Y. Sugahara, T. Tachiba, and H. Toki, Nucl. Phys. **A616**, 438 (1997).
  - [28] G.A. Lalazissis, S. Raman, and P. Ring, At. Data. Nucl. Data Tables **71**, 1 (1999).
  - [29] N. Sandulescu, N. Van Giai, and R.J. Liotta, Phy. Rev. C **61**, 061301(R) (2000).
  - [30] L.S. Geng, H. Toki, S. Sugimoto, and J. Meng, Prog. Theor. Phys. **110**, 921 (2003).
  - [31] L.S. Geng, H. Toki, and J. Meng, Prog. Theor. Phys. **113**, 785 (2005).
  - [32] H. Geissel, et al., AIP Conference Proceedings, **831**, 108 (2006).
  - [33] G. Audi, A.H. Wapstra, and C. Thibault, Nucl. Phys. **A729**, 337 (2003).
  - [34] P. Marmier, and E. Sheldon, *Physics of Nuclei and Particles*, vol. I, Academic Press, New York, 1971.
  - [35] S.E. Woosley, and R.D. Hoffman, Astrophys. J. **395**, 202 (1992).
  - [36] K. Takahashi, J. Witt, and H.-Th. Janka, Astro. and astrophys. **286**, 857 (1994).
  - [37] S. Wanajo, T. Kajino, G.J. Mathews, and K. Otsuki, Astrophys. J. **554**, 578 (2001).
  - [38] T.A. Thompson, A. Burrows, and B.S. Meyer, Astrophys. J. **562**, 887 (2001).
  - [39] C. Freiburghaus, S. Rosswog, and F.-K. Thielemann, Astrophys. J. **525**, 121 (1999).
  - [40] S. Rosswog, M. Liebendörfer, F.-K. Thielemann, M.B. Davies, W. Benz, and T. Piran, Astro. and astrophys. **341**, 499 (1999).
  - [41] S. Goriely, P. Demetriou, H.-Th. Janka, J.M. Pearson, and M. Samyn, Nucl. Phys. **A758**, 587 (2005).
  - [42] A.G.W. Cameron, Astrophys. J. **562**, 456 (2001).
  - [43] Ning, H., Qian, Y.-Z., & Meyer, B.S., Astrophys. J. Lett. **667**, L159 (2007).

- [44] R. Surman, and G.C. McLaughlin, Nucl. Phys. **A758**, 189 (2005).
- [45] J.J. Cowan, J.E. Lawler, C. Sneden, E.A.D. Hartog, and J. Collier, *in proceedings of the NASA Laboratory Astrophysics Workshop*, ed. P.F. Weck, H.S. Kwong, and F. Salama, 82 (2006).
- [46] K.-L. Kratz, K. Farouqi, B. Pfeiffer, J.W. Truran, C. Sneden, and J.J. Cowan, Astrophys. J. **662**, 39 (2007).
- [47] J.J. Cowan, B. Pfeiffer, K.-L. Kratz, F.-K. Thielemann, C. Sneden, S. Burles, D. Tyler, and T.C. Beers, Astrophys. J. **521**, 194 (1999).
- [48] F. Käppeler, H. Beer, and K. Wisshak, Rep. Prog. Phys., **52**, 945 (1989).
- [49] P. Möller, J.R. Nix, and K.-L. Kratz, At. Data Nucl. Data Tables **66**, 131 (1997); P. Möller, B. Pfeiffer, and K.-L. Kratz, Phys. Rev. C **67**, 055802 (2003).
- [50] National Nuclear Data Center, <http://www.nndc.bnl.gov>.
- [51] B. Chen, J. Dobaczewski, K.-L. Kratz, K. Langanke, B. Pfeiffer, F.-K. Thielemann, and P. Vogel, Phys. Lett. **B355**, 37 (1995).
- [52] H. Schatz, R. Toenjes, B. Pfeiffer, T.C. Beers, J.J. Cowan, V. Hill, and K.-L. Kratz, Astrophys. J. **579**, 626 (2002).
- [53] K. Farouqi, et al., Nucl. Phys. **A758**, 631c (2005).
- [54] I. Dillmann, et al., Phys. Rev. Lett. **91**, 162503 (2003).
- [55] W.B. Walters, et al., Phys. Rev. C **70**, 034314 (2004).
- [56] A. Jungclaus, et al., Phys. Rev. Lett. **99**, 132501 (2007).
- [57] C. Travaglio, R. Gallino, E. Arnone, J. Cowan, F. Jordan, and C. Sneden, Astrophys. J. **601**, 864 (2004).
- [58] F. Montes, et al., Astrophys. J. **671**, 2, 1685 (2007).
- [59] B. Sun, and J. Meng, Chin. Phys. Lett., **25**, 2429 (2008).

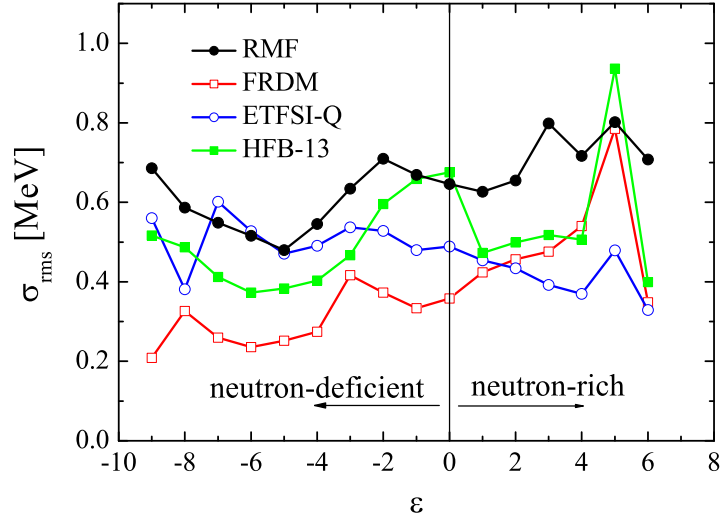


FIG. 1: (Color online) The *rms* deviation  $\sigma_{rms}$  of one-neutron separation energy  $S_n$  with respect to experimental data [33] as a function of the distant from the  $\beta$ -stability line  $\varepsilon = Z_0 - Z$  for different mass models, where  $Z_0$  stands for the proton number of the most stable isotope in the isobaric chain with mass number  $A$ .



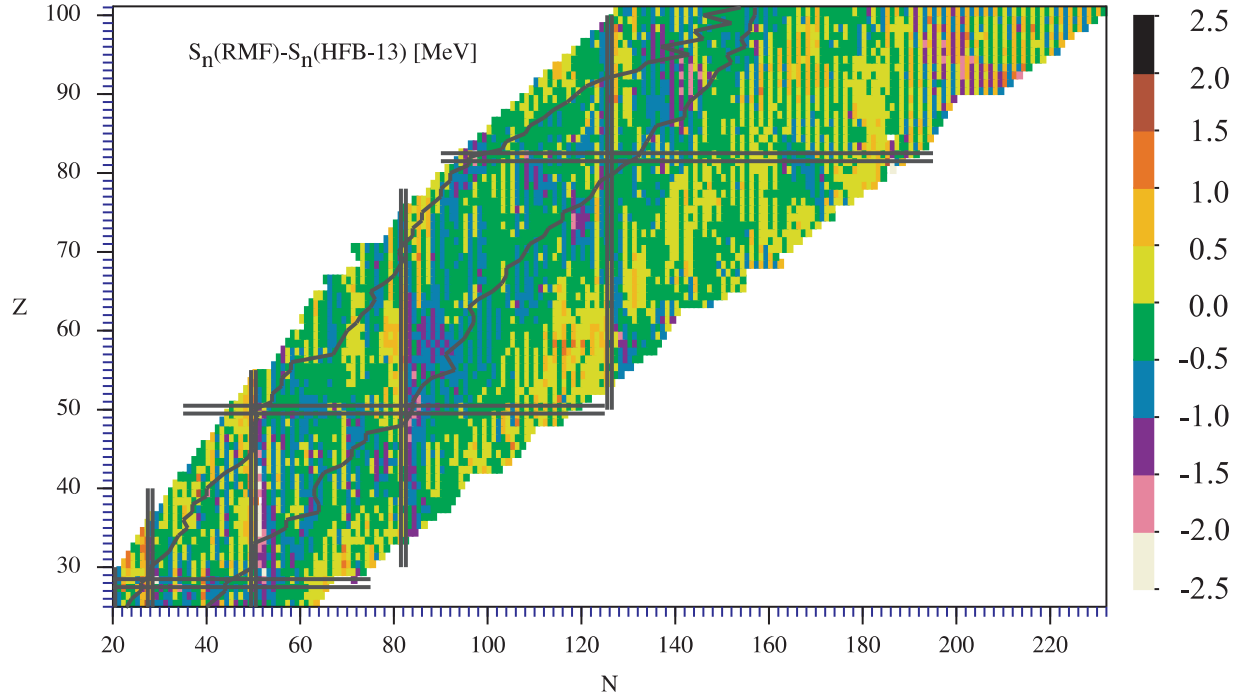


FIG. 2: (Color online) The differences between one neutron separation energies  $S_n$  predicted in the RMF model and those in the HFB-13 model. The magic proton and neutron numbers are indicated by pairs of parallel lines, and also the present border of the data with known masses are shown by solid lines.

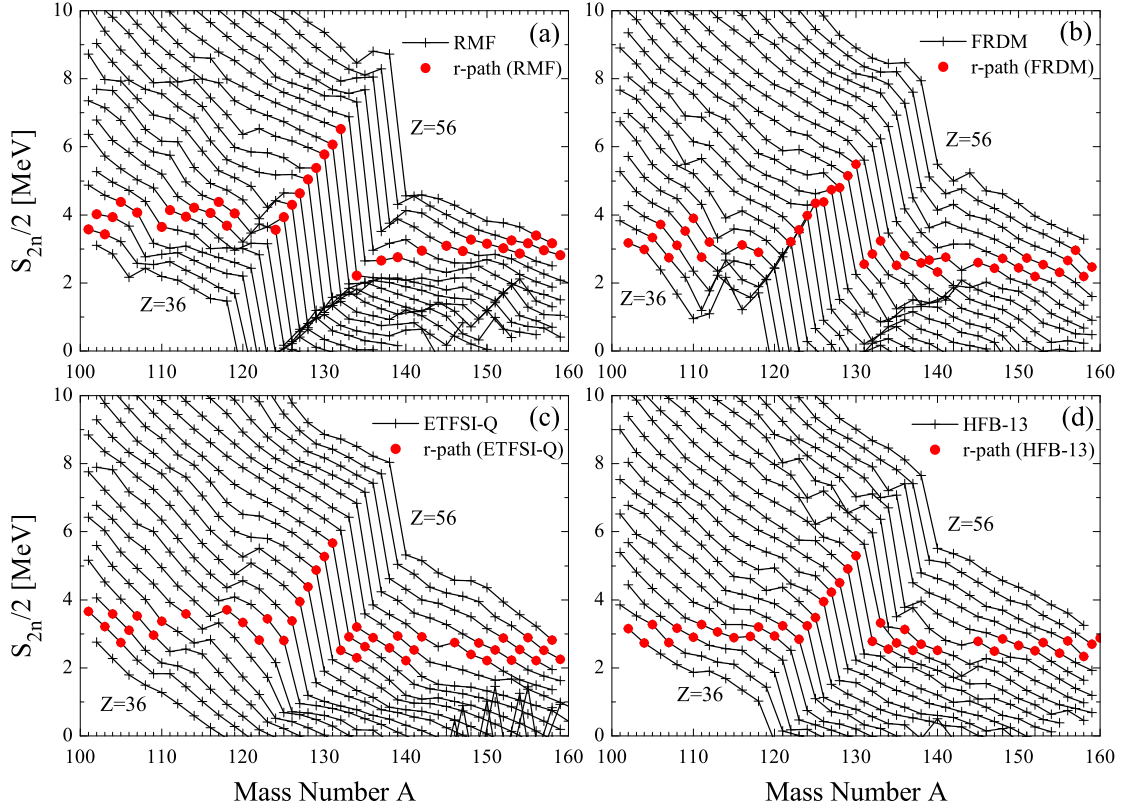


FIG. 3: (Color online) The average one-neutron separation energies around the  $N = 82$  shell in the RMF model, in comparison with those in the FRDM, ETFSI-Q and HFB-13 models as a function of mass number  $A$ . For simplicity only nuclei with even  $N$  are plotted. The corresponding  $r$ -process paths calculated using different mass inputs are also indicated by dots, and labeled here are those isotopes with more than 10% population of each isotopic chain.

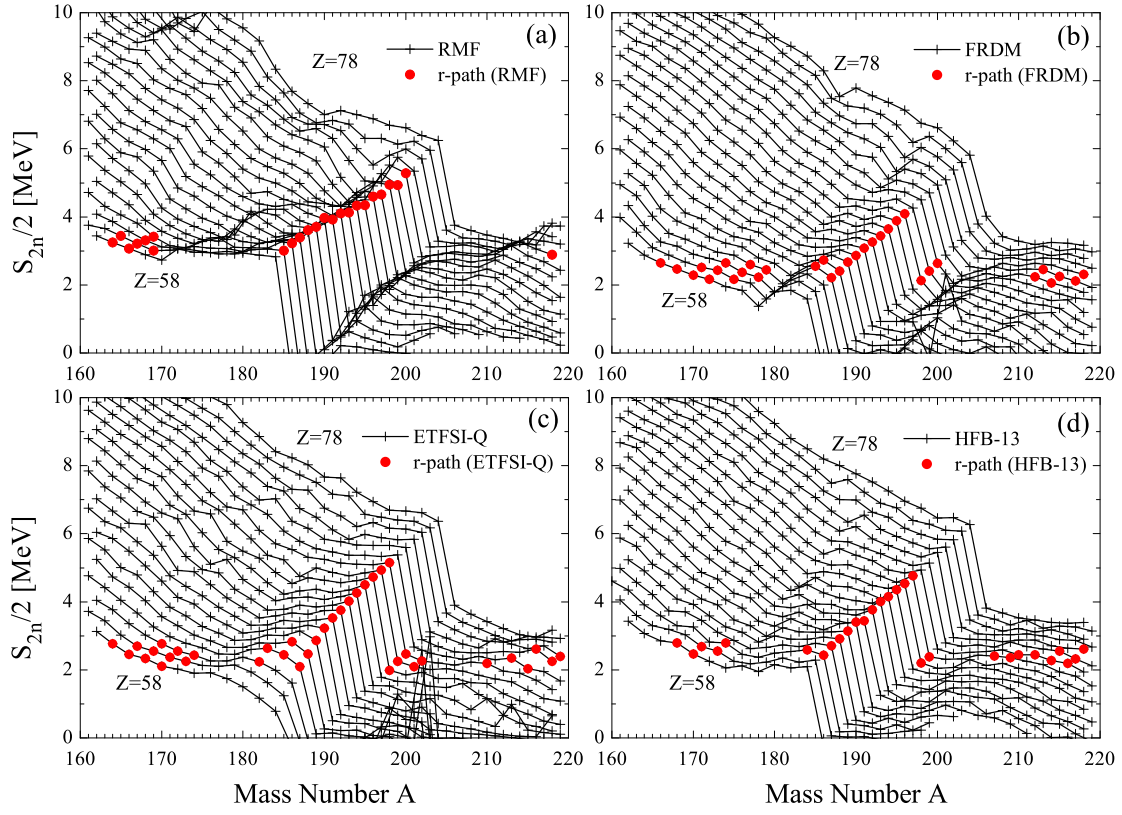


FIG. 4: (Color online) Same to Fig. 3 but around the  $N = 126$  shell.

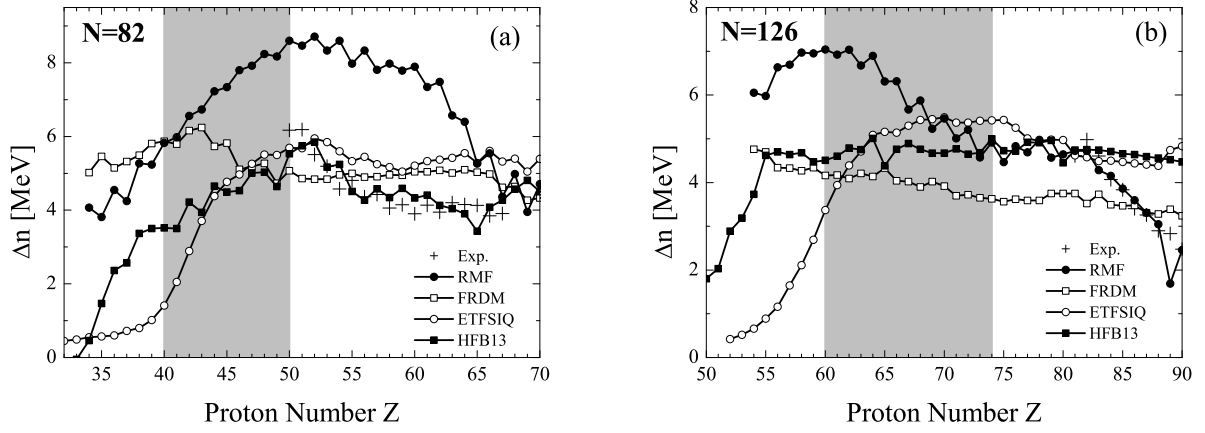


FIG. 5: The neutron shell gaps  $\Delta_n(Z, A) = S_{2n}(Z, A) - S_{2n}(Z, A + 2)$  for  $N = 82$  and  $126$  in the RMF approach compared with those in the FRDM, ETFSI-Q and HFB-13 models together with the data available. The nuclei in the shadowed areas are involved in the  $r$ -process paths based on our calculations.

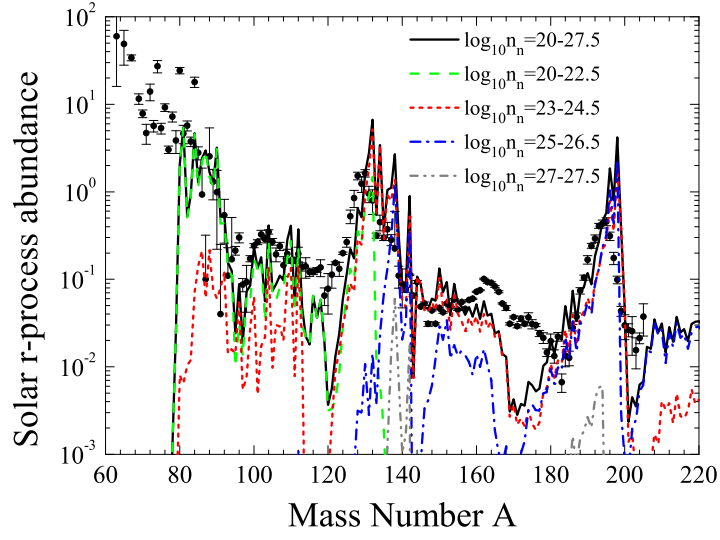


FIG. 6: (Color online) The effect of various weighted  $r$ -process components on the resulting fit after  $\beta$ -decays in the best superposition using the RMF masses. The calculated total isotopic abundances (in the logarithm scale)) is normalized to  $A = 130$ .

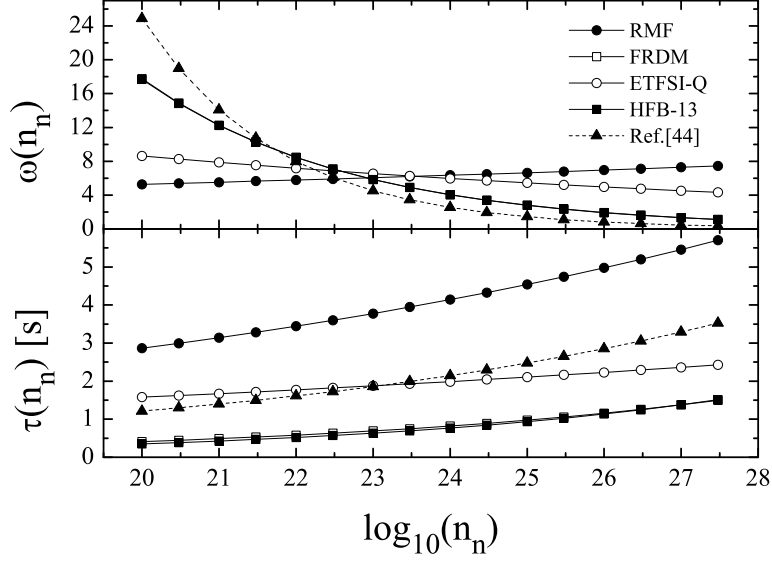


FIG. 7: The best configuration of sixteen  $r$ -process components which reproduce the solar system  $r$ -process abundances with different mass inputs at the temperature  $T = 1.5$  GK. The neutron density  $n_n$  is in the unit of  $\text{cm}^{-3}$ . The weighting factor  $\omega(n_n)$  and the neutron irradiation time  $\tau(n_n)$  are shown in the upper and lower panels as a function of neutron density  $n_n$ . In the upper panel, the weighting factors for the FRDM are completely overlaid by those for the HFB-13 models. The fit from Ref. [47] is also plotted for comparison. The total weighting factor has been normalized to 100.

TABLE I: Our best fits to the solar  $r$ -process abundances for different sets of nuclear mass models. The first column is the mass model employed. The last two columns are the weight  $\omega$  and the relevant neutron irradiation time  $\tau$  (in unit of second), respectively.

Mass model	$\omega$	$\tau$ [s]
RMF	$2.1 \times n_n^{0.020}$	$0.454 \times n_n^{0.040}$
FRDM	$3.0\text{E}4 \times n_n^{-0.161}$	$0.013 \times n_n^{0.075}$
ETFSI-Q	$54.4 \times n_n^{-0.040}$	$0.499 \times n_n^{0.025}$
HFB13	$2.8\text{E}4 \times n_n^{-0.160}$	$0.007 \times n_n^{0.085}$

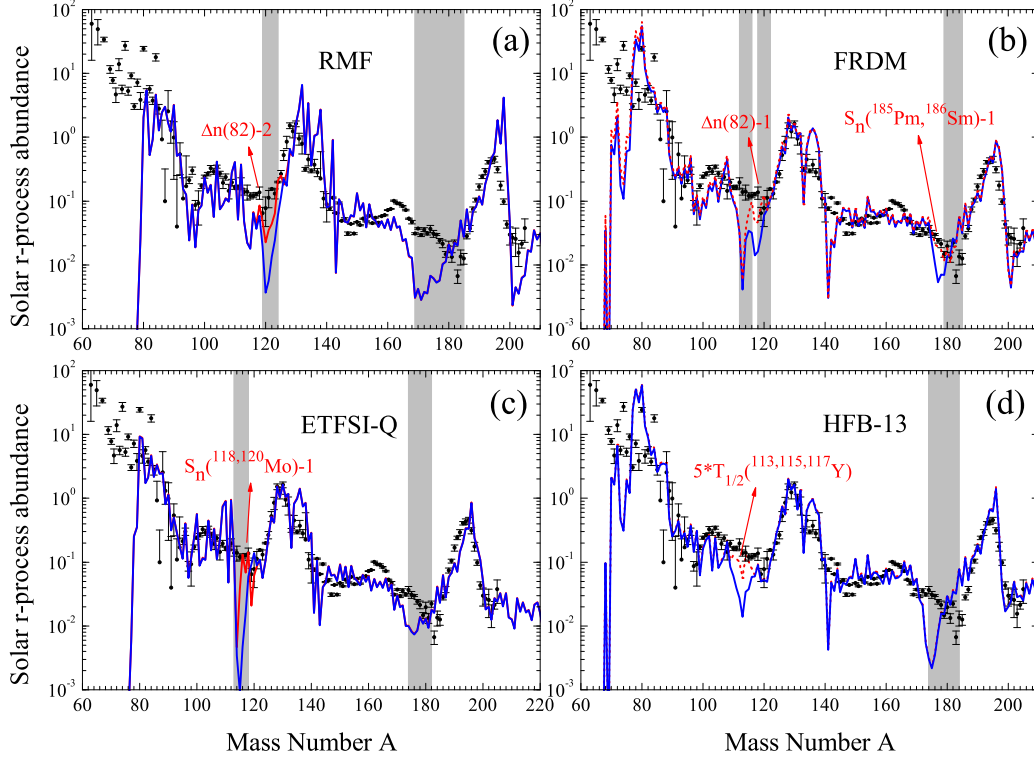


FIG. 8: (Color online) Our best fits to the solar  $r$ -process abundances (in the logarithm scale) under different nuclear mass inputs. The  $\beta$ -decay properties are taken from the FRDM model [49]. The best fits are displayed as blue-solid lines. In the sub-figure (a), the red-dashed curve is the same as the blue-solid curve but with a shell closure at  $N = 82$  2 MeV smaller. In the sub-figure (b), the red-dashed curve is the same as the blue-solid curve but with a shell closure at  $N = 126$  1 MeV smaller and separation energies of  $^{185}\text{Pm}$  and  $^{186}\text{Sm}$  1 MeV smaller. In the sub-figure (c), the red-dashed curve is the same as the blue-solid curve but with separation energies of  $^{185}\text{Pm}$  and  $^{118,120}\text{Sn}$  1 MeV smaller. In the sub-figure (d), the red-dashed curve is the same as the blue-solid curve but with half-life of isotopes  $^{113,115,117}\text{Y}$  five times larger. The shadowed areas correspond to the range where the abundances of these isotopes are largely underestimated before neutrons freeze out.